Polarization-dependent near-field phonon nanoscopy of oxides: $SrTiO_3$, $LiNbO_3$, and $PbZr_{0.2}Ti_{0.8}O_3$

Lukas Wehmeier,[1,*] Denny Lang,[2] Yongmin Liu,[3,4,5] Xiang Zhang,[5] Stephan Winnerl,[2]
Lukas M. Eng,[1,6] and Susanne C. Kehr[1,†]

[1]*Institute of Applied Physics, Technische Universität Dresden, 01062 Dresden, Germany*
[2]*Institute of Ion Beam Physics and Materials Research, Helmholtz-Zentrum Dresden-Rossendorf, 01328 Dresden, Germany*
[3]*Department of Mechanical and Industrial Engineering, Northeastern University, Boston, Massachusetts 02115, USA*
[4]*Department of Electrical and Computer Engineering, Northeastern University, Boston, Massachusetts 02115, USA*
[5]*Department of Mechanical Engineering, University of California, Berkeley, California 94720, USA*
[6]*ct.qmat, Dresden-Würzburg Cluster of Excellence - EXC 2147, TU Dresden, 01062 Dresden, Germany*

(Received 30 March 2019; revised manuscript received 5 July 2019; published 29 July 2019)

Resonant infrared near-field optical spectroscopy provides a highly material-specific response with subwavelength lateral resolution of ∼10 nm. Here, we report on the study of the near-field response of selected paraelectric and ferroelectric materials, i.e., $SrTiO_3$, $LiNbO_3$, and $PbZr_{0.2}Ti_{0.8}O_3$, showing resonances in the wavelength range from 13.0 to 15.8 μm. We investigate these materials using scattering scanning near-field optical microscopy in combination with a tunable mid-infrared free-electron laser. Fundamentally, we demonstrate that phonon-induced resonant near-field excitation is possible for both *p*- and *s*-polarized incident light, a fact that is of particular interest for the nanoscopic investigation of anisotropic and hyperbolic materials. Moreover, we exploit that near-field spectroscopy, as compared to far-field techniques, bears substantial advantages such as lower penetration depths, stronger confinement, and a high spatial resolution. The latter permits the investigation of minute material volumes, e.g., with nanoscale changes in crystallographic structure, which we prove here via near-field imaging of ferroelectric domain structures in $PbZr_{0.2}Ti_{0.8}O_3$ thin films.

DOI: 10.1103/PhysRevB.100.035444

I. INTRODUCTION

Optical resolution at nanometer sizes is highly desired for the investigation of naturally occurring and biological samples [1], as well as for analyzing artificially assembled materials such as electronic or optical nanostructures [2,3]. Particularly, unique material responses are found in the *so-called* optical "fingerprint region" at wave numbers $\tilde{\nu}$ between 600 and 1500 cm^{-1} [4], a range that is easily accessible with Fourier-transform infrared (FTIR) and Raman spectroscopy. These techniques, however, are typically limited by optical diffraction, which implies that spatial resolution in infrared microscopy stays far from the nanometer range or single object information.

Apertureless near-field techniques such as tip-enhanced Raman spectroscopy (TERS) [5,6] as well as scattering scanning near-field optical microscopy (s-SNOM) [7–10] and spectroscopy (nano-FTIR [1,11]) overcome the diffraction limit by combining far-field techniques with optical field enhancement, e.g., using an atomic force microscope (AFM) tip. Remarkably, s-SNOM is applicable to arbitrary sample materials without the need of vacuum, conductive coating, or additional sample labeling, as necessary in other high-resolution microscopy techniques [12–15]. Wavelength-independent spatial resolution in the order of ∼10 nm has been demonstrated via s-SNOM and nano-FTIR for different material systems, such as metal/nonmetal structures [16–19], organic [16,20] and biological materials [1,21,22], semiconductors [18,23], and ferroelectric domain structures [24–27].

Close to material resonances such as plasmon and phonon modes, signal strength and material contrast in s-SNOM can be strongly enhanced [17,24–31]. At infrared wavelengths, this mechanism is highly sensitive to the material properties and may be applied to polar materials [28,31], metals, semiconductors [18,23], and biological samples [1,21,22]. Resonant excitation even allows for the local characterization within the very same material, e.g., of local stress distribution [31], polytypism [32], dopant and charge carrier concentration [18,23,33,34], or change in anisotropy tensor orientation [24–27]. In general, strong near-field resonances have been observed for various crystalline structures [17,24–31,34–38], indicating that spectroscopic near-field material analysis is applicable to a manifold of different material types that await to be inspected at the nanometer length scale.

In far-field microscopy, polarization-sensitive measurements such as ellipsometry, yield valuable additional sample information, e.g., the optical anisotropy [39]. In aperture-SNOM, the role of polarization has been early recognized [40]. In *scattering*-SNOM, it is often assumed that *s*-polarized near-field contributions may be neglected due to the tip-sample *p*-polarized dominance [41,42]. Nevertheless, in the past decade *s*-polarized measurements have been utilized to study metal and semiconductor nanostructures, both in the visible [43–46] and in the infrared regimes [2,3,47–52]. Particularly, a cross-polarization scheme has been employed for background suppression of far-field contributions [2] and

*lukas.wehmeier@tu-dresden.de
†susanne.kehr@tu-dresden.de

polarization-dependent s-SNOM was applied for nonlinear optical mapping of ferroelectric domains [53]. However, to the best of our knowledge, polarization dependence has not been explored for sample-resonant near-field excitation. Note that resonant near-field analysis fundamentally enables polarization-sensitive probing in s-SNOM.

Materials with perovskite or perovskitelike structure show a multitude of fascinating and most diverse material properties [54–56], such as piezoelectricity, pyroelectricity, paraelectricity, ferroelectricity, and antiferroelectricity [54–56], (anti)ferromagnetism [57], multiferroicity [57–60], high dielectric permittivity [58], hyperbolic dispersion [39], high electro-optic coefficients [59,61], nonlinear optical response [54,59,62], colossal magnetoresistance [63], superconductivity [64,65], and resistive switching [66]. Correspondingly, an immense spectrum of applications exists, including pyroelectric detectors [56], piezoelectric actuators [56], light-emitting diodes and lasers [67], solar cells [68], nonlinear optics [54,62,69], ferroelectric and resistive random access memory (FeRAM [56] and RRAM [70]), and multiferroic memory devices and spintronics [60]. For all these technological applications, a nanoscale and fundamental characterization of their material properties is essential. Of the inorganic perovskites, oxides may be considered the most important subgroup, showing almost any of the above-mentioned properties [39,54–57,59–62,64–66,70–72]. Near-field microscopy on such systems shows strong phonon-enhanced resonances [24–26,30,34–38] that have, e.g., been applied in superlens structures [35,38]. However, so far, s-SNOM studies solely included *p*-polarized light excitation, while the polarization influence remains unexplored. We thus will focus on perovskite oxides in this study as a model system with exceptional technological relevance.

We discuss resonant near-field enhancement in both theory (Sec. II) and experiment (Sec. III) and demonstrate a highly characteristic material response for both *s*- and *p*-polarized illumination. Utilizing a narrow-band mid-infrared free-electron laser (FEL), we experimentally confirm the applicability of polarization-sensitive s-SNOM to various perovskite oxides of increasing structural complexity (Sec. III A). We demonstrate of resonant responses for two bulk samples: isotropic, model perovskite oxide $SrTiO_3$ and anisotropic, perovskitelike [56] $LiNbO_3$ at their highest-energy phonon resonances for both *p*- and *s*-polarized incident light. The obtained near-field characteristics are compared with far-field FTIR spectra, which present a reference for our near-field investigations at infrared wavelengths. When investigating a thin-film perovskite, $PbZr_{0.2}Ti_{0.8}O_3$ (PZT), with the same methods we show that near-field spectroscopy allows for material characterization with negligible influence of the substrate. Moreover, we verify the lateral resolution of the technique by probing the ferroelectric domain structure in a PZT thin film (Sec. III B).

II. THEORETICAL APPROACH

A. Comparing theoretical model descriptions

Various analytical [24,73–78] and numerical [79–81] models exist to describe the near-field response of a certain material, including its dependence on wavelength and tip-sample distance. However, field components parallel to the sample surface, i.e., *s* polarized, are mostly neglected [75–80] due to the reduced near-field response for off-resonant excitation and the tip's lower polarizability as compared to on-axis, i.e., *p*-polarized, excitation. Some models, such as the finite-dipole model [76] or the lightning-rod model [77], do not even allow for polarization other than *p* polarization due to their inherent axial symmetry [76,77], which would be broken for non-*p*-polarized light. Note that for the theoretical description we use *p* and *s* polarization for polarization either parallel or perpendicular to the sample normal, which differs from the conventional description used in experiments Sec. III, where *p* or *s* polarization is given with respect to the incident plane.

In the following Sec. II B, we apply the analytical dipole model [16,74] for qualitative predictions: The dipole model is an electrostatic model, where the s-SNOM tip is approximated by a point dipole, while the near-field coupling is described via interaction with a mirror dipole within the sample. A more detailed introduction is given in Appendix A. The dipole model has many advantages like being simple, intuitive, well established [1,11,78,81,82], and building the basis for more advanced analytical descriptions [24,75,78]. Simplifications within the dipole model lead to some well-studied inaccuracy, e.g., a too fast dropoff of the near-field signal with increasing tip-sample distance [75–77]. However, in contrast to most other models, the dipole model directly accounts for both *s*- and *p*-polarized incident light [74], which is the main reason for using it here.

B. Predictions of the dipole model

Using the dipole model including higher-harmonic demodulation [28,74] (for a detailed description, see Appendix A), we calculate different properties of a model material that shows a transverse optical phonon resonance at $\tilde{\nu}_{\mathrm{TO}} = 500\ \mathrm{cm}^{-1}$ (i.e., at $\lambda_{\mathrm{TO}} = 20.0\ \mu\mathrm{m}$ or 15.0 THz, with damping constant $\gamma_{\mathrm{TO}} = 50\ \mathrm{cm}^{-1}$), longitudinal optical (LO) mode at $\tilde{\nu}_{\mathrm{LO}} = 750\ \mathrm{cm}^{-1}$ (i.e., $\lambda_{\mathrm{LO}} = 13.3\ \mu\mathrm{m}$ or 22.5 THz, with damping $\gamma_{\mathrm{LO}} = 50\ \mathrm{cm}^{-1}$), and a high-frequency optical permittivity $\epsilon_\infty = 5.0$. Figure 1(b) shows the resulting reflectivity of this sample, including a region of high reflectivity from 13.3 to 20.0 μm corresponding to the phonon mode's reststrahlenband. Matching the wavelength regimes of Figs. 1(b) and 1(e), 1(f), 1(h), and 1(i), respectively, Figs. 1(c), 1(d), and 1(g) depict the complex permittivity [83]

$$\epsilon = \epsilon' + i\epsilon'' = \epsilon_\infty \frac{\tilde{\nu}_{\mathrm{LO}}^2 - \tilde{\nu}^2 + i\gamma_{\mathrm{LO}}\tilde{\nu}}{\tilde{\nu}_{\mathrm{TO}}^2 - \tilde{\nu}^2 + i\gamma_{\mathrm{TO}}\tilde{\nu}}. \tag{1}$$

The region of negative ϵ' corresponds to the reststrahlenband. Figures 1(e), 1(f), 1(h), and 1(i), finally, show the dipole model's prediction for the near-field signal for *p*- and *s*-polarized illumination, respectively. Here, the near-field signal is plotted as a function of tip-sample distance and wavelength in the regime of the near-field resonance. Note that in our experimental setup (details described in Appendix B) we implement a self-homodyne detection scheme [74], that is also fully considered and integrated into our theoretical description (for details see Appendix A). Particularly for

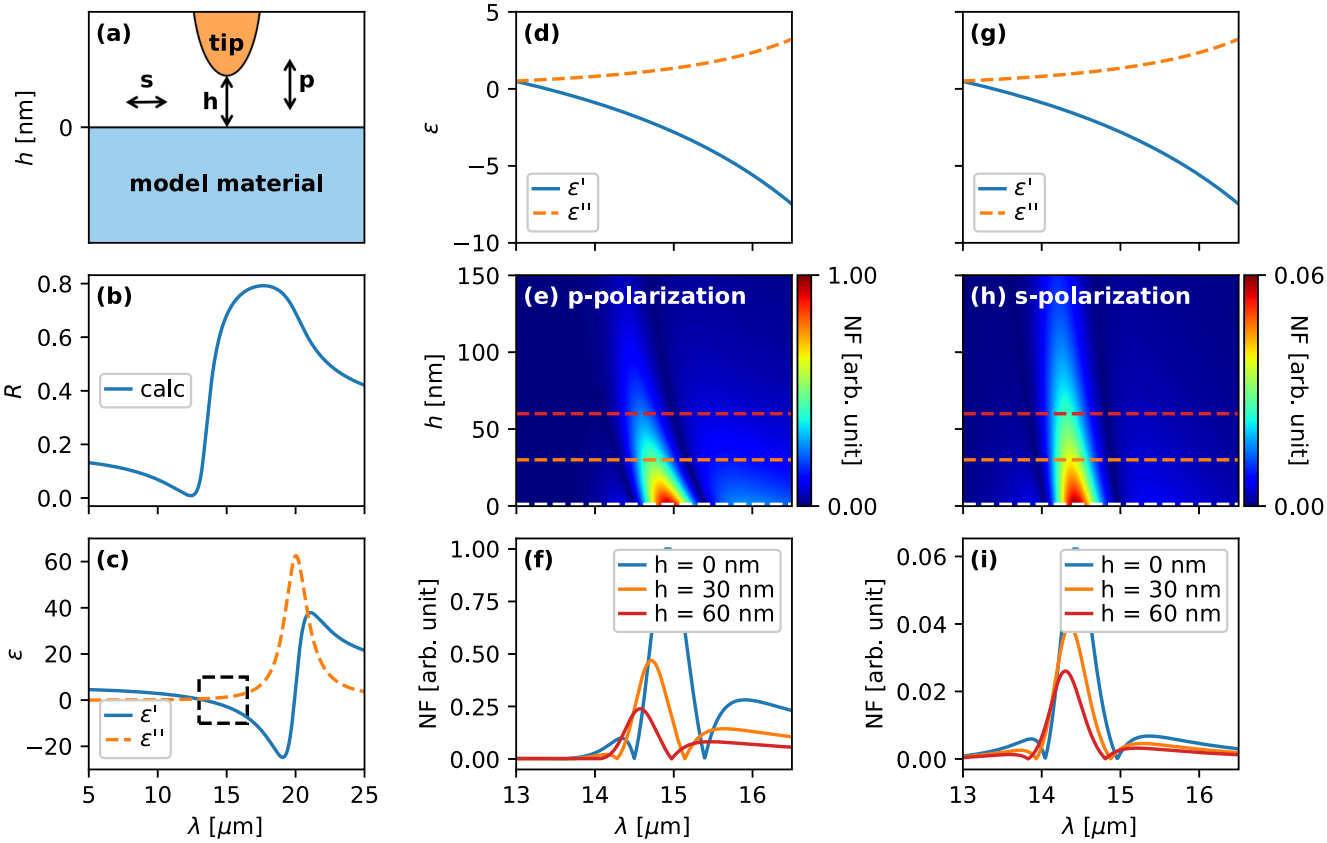

FIG. 1. Far- and near-field response of a model material having a single phonon resonance with a TO mode at 20.0 μm and a LO mode at 13.3 μm: (a) Simplified sketch of the s-SNOM setup, consisting of sample and tip. Note the definition of *p*- and *s*-polarized light. (b) Far-field reflectivity R at the phonon resonance and (c) real and imaginary parts of the permittivity ϵ' and ϵ''. (d), (g) Permittivity for a smaller wavelength regime from 13.0–16.5 μm (see box in c), matching (e), (f) and (h), (i). (e), (h) Calculated near-field signal NF as a function of tip-sample distance h and wavelength λ; in (e) and (f) the illuminating light is *p* polarized, in (h) and (i) it is *s* polarized. For comparison, NF is normalized to the maximum value for *p* polarization. (f), (i) Spectra for tip-sample distances of $h = 0$, 30, and 60 nm corresponding to the dashed lines in (e) and (h). Please note that the same figure layout is used for experimental results reported in Figs. 2–4.

self-homodyne detection, the measured near-field signal includes both the near-field amplitude and phase, which are measured separately in most commercial s-SNOM setups.

The dipole model illustrates many of the features that are observed in near-field experiments (Sec. III A):

(i) At resonance, the near-field response is strongly increased due to phonon-enhanced light-matter interaction [28]. Here, for *p*-polarized light [Figs. 1(e) and 1(f)] we expect an almost 10-fold amplification in comparison to a gold reference sample. For *s* polarization [Figs. 1(h) and 1(i)], the amplification is three to four orders of magnitude compared to gold, resulting in about 6% of the response for *p* polarization. Note that for nonresonant excitation the signal strength for *s* polarization is typically about five orders of magnitude smaller as compared to *p* polarization.

(ii) The near-field resonances are spectrally sharper in comparison to the far-field response (reflectivity) [Fig. 1(b)] [28], and are blue-shifted when referenced to the absorption maximum of the phonon resonance [24].

(iii) Whereas nonresonant samples typically show a monotonously decreasing near-field intensity with increasing tip-sample distance h, local maxima may occur at specific distances when analyzing resonant samples [24,30,78,81,84], e.g., at 14.6 μm in Figs. 1(e) and 1(f) and at 14.2 μm in Figs. 1(h) and 1(i).

(iv) The resonance for *p*-polarized illumination occurs for ϵ' from -7 to -1 with two maxima, a stronger maximum $\lambda_{\max,p,1} \approx (14.9 \pm 0.1)$ μm (i.e., 671 cm^{-1} or 20.1 THz), corresponding to $\epsilon' \approx -2.6 \pm 0.3$, and a weaker one at $\lambda_{\max,p,2} \approx (15.9 \pm 0.1)$ μm (i.e., 629 cm^{-1} or 18.9 THz), corresponding to $\epsilon' \approx -5.3 \pm 0.4$. However, these values of ϵ' depend on the imaginary part, too: In general, a larger imaginary part of the permittivity ϵ'' broadens the resonance, shifts the local maximum in the near-field response to more negative ϵ', and decreases the maximum amplitude [17,29]. Please note that the self-homodyne detection scheme considered in our theoretical description introduces additional maxima/minima not present in most other detection schemes.

(v) With increasing tip-sample distance, the resonance blue-shifts toward $\epsilon' = -1$ [24,30,84], which leads to the characteristic bended, lobelike structure as depicted in Figs. 1(e) and 1(h).

(vi) The near-field resonance for *s*-polarized incident light is slightly blue-shifted in comparison to the *p*-polarized case, and appears in the range of $-3 \leqslant \epsilon' \leqslant -1$, with a maximum at $\lambda_{\max,s} \approx (14.4 \pm 0.1)$ μm (i.e., 694 cm^{-1} or 20.8 THz),

corresponding to $\epsilon' \approx -1.6 \pm 0.3$. Otherwise, it shows similar general characteristics, especially the lobelike structure and the shift toward $\epsilon = -1$ for large tip-sample distances h.

III. EXPERIMENTAL RESULTS

This section is structured into two subsections: In Sec. III A we present measured near-field spectra, providing examples of different material classes with increasing complexity. Specifically, we investigate two bulk materials:

(i) strontium titanate ($SrTiO_3$; STO), a paraelectric perovskite at room temperature [55], that is widely used as a highly crystalline substrate for thin-film growth of inorganic perovskites [56,57,59,72]; it forms the basis for a large group of materials used for resistive switching applications [66];

(ii) lithium niobate ($LiNbO_3$; LNO), a trigonal, but perovskitelike, uniaxial ferroelectric [54,56], also called the "silicon of ferroelectrics"; LNO is mostly used in bulk and surface acoustic wave devices [85] and nonlinear optics [62,69], e.g., for second-harmonic generation;

as well as a thin film oxide:

(iii) lead zirconate titanate ($PbZr_{0.2}Ti_{0.8}O_3$; PZT), a ferroelectric perovskite [54–56,86] thin film that is widely used as a piezoelectric actuator [56].

While spectroscopic s-SNOM measurements already provide a spatial resolution of ∼10 nm, this is in general not apparent in point spectroscopy. Therefore, in Sec. III B we show optical near-field images of the ferroelectric domain structure of PZT, demonstrating the high spatial resolution of the method.

For investigation of the near-field response of these oxide: systems, we use a home-built s-SNOM applying a self-homodyne detection scheme [74], in combination with free-electron laser illumination [24,35]. This setup allows us to access the near-field responses at any wavelength in the mid- to far-infrared wavelength regime from 5–250 μm, i.e., 40–2000 cm^{-1} or 1.2–60.0 THz. The incident light is linearly polarized and hits the tip-sample junction either "p" or "s" polarized, respectively, using Gaussian optics that partly turns the polarization, but maintains its orthogonality. Note that both the focusing of the light and reflection on the sample and the microscope (including the tip) may introduce polarization mixing. For details on the experimental setup, see Appendix B.

A. Characteristic near-field spectra of the highest-energy phonon mode

Due to the similar crystallographic structure of the selected materials, their highest-energy phonon modes are found in the same wavelength range with their λ_{TO} within <10% around $\lambda \approx 17.4$ μm, i.e., 575 cm^{-1} or 17.2 THz. For all materials, ϵ was calculated from literature phonon data using

$$\epsilon = \epsilon' + i\epsilon'' = \epsilon_\infty \prod_{m=1}^{n} \frac{\tilde{\nu}_{m,\mathrm{LO}}^2 - \tilde{\nu}^2 + i\gamma_{m,\mathrm{LO}}\tilde{\nu}}{\tilde{\nu}_{m,\mathrm{TO}}^2 - \tilde{\nu}^2 + i\gamma_{m,\mathrm{TO}}\tilde{\nu}}, \qquad (2)$$

with n the number of contributing phonon modes [83]. The corresponding reflectivity is compared with experimentally obtained FTIR data. According to the dipole model (Fig. 1), the near-field resonance is expected at wavelengths slightly red-shifted with respect to phonon-induced zero crossing of ϵ', i.e., within the reststrahlenbands of the phonon modes. For all materials such near-field resonances are explored utilizing both p and s polarization.

1. Strontium titanate (STO)

The first material we present here is undoped bulk (100)-STO, with its highest energy phonon TO mode at $\lambda_{TO} = 18.2$ μm (i.e., 548 cm^{-1} or 16.5 THz, with $\gamma_{TO} = 11$ cm^{-1}), the corresponding LO mode at $\lambda_{LO} = 12.6$ μm (i.e., 795 cm^{-1} or 23.8 THz with $\gamma_{LO} = 35$ cm^{-1}) [87], and $\epsilon_\infty = 5.2$ [88,89]. The STO sample was purchased from CrysTec, Germany.

Figure 2(b) shows the measured far-field reflectivity obtained by FTIR. Applying a constant scaling factor allows us to perfectly correlate our measurement with the reflectivity spectrum calculated from literature data [87]. Figure 2(c) shows ϵ for the same wavelength range. Clearly, in Fig. 2(b), the region of high reflectivity corresponds to the region with $\epsilon' < 0$. Figures 2(d) and 2(g) show ϵ in the regime that is relevant for interpreting our near-field data shown in Figs. 2(e), 2(f), 2(h), and 2(i).

For p-polarized incident light [Figs. 2(e) and 2(f)] and $h = 0$, i.e., tip and sample in feedback, maximum near-field response is observed for $\lambda_{\max,p} \approx (14.9 \pm 0.1)$ μm (i.e., 671 cm^{-1} or 20.1 THz), corresponding to $\epsilon' \approx -3.2 \pm 0.2$. Recently, the near-field resonance of STO was investigated via nano-FTIR using broadband illumination [34,36,37]. Albeit our near-field signal presents a combined response of near-field amplitude and phase due to the self-homodyne detection scheme, $\lambda_{\max,p}$ may be compared to the wavelength of maximum near-field amplitude observed in these measurements, which is 15.6 μm (640 cm^{-1}) [37], 15.1 μm (663 cm^{-1}) [36], and 15.2 μm (660 cm^{-1}) [34], respectively, with the latter studying a 0.3%-La-doped STO ceramic.

For s-polarized illumination [Figs. 2(h) and 2(i)] and $h = 0$, the near-field resonance occurs at slightly longer wavelengths as compared to p polarization, with a local maximum at $\lambda_{\max,s} \approx (15.3 \pm 0.1)$ μm (i.e., 658 cm^{-1} or 19.7 THz), corresponding to $\epsilon' \approx -4.1 \pm 0.3$. When increasing the tip-sample distance, the near-field resonances for both p- and s-polarized incident light shift to shorter wavelengths, which results in the characteristic bending of the near-field resonance lobes in perfect accordance to the dipole model.

Comparing the maximum near-field response observed for both polarizations within the wavelength range shown in Figs. 2(e), 2(f), 2(h), and 2(i), we find a ratio of 0.53 between s and p polarization. Yet, the behavior observed in Figs. 2(h) and 2(i) suggests that even stronger near-field enhancement may be observable for s polarization at this phonon mode for $\lambda \geqslant 16.0$ μm, i.e., outside of the wavelength range measured here.

2. z-cut lithium niobate (LNO)

While STO is optically isotropic, LNO is uniaxial and birefringent, which leads to different phonon wavelengths, depending on the polarization of the incoming light with

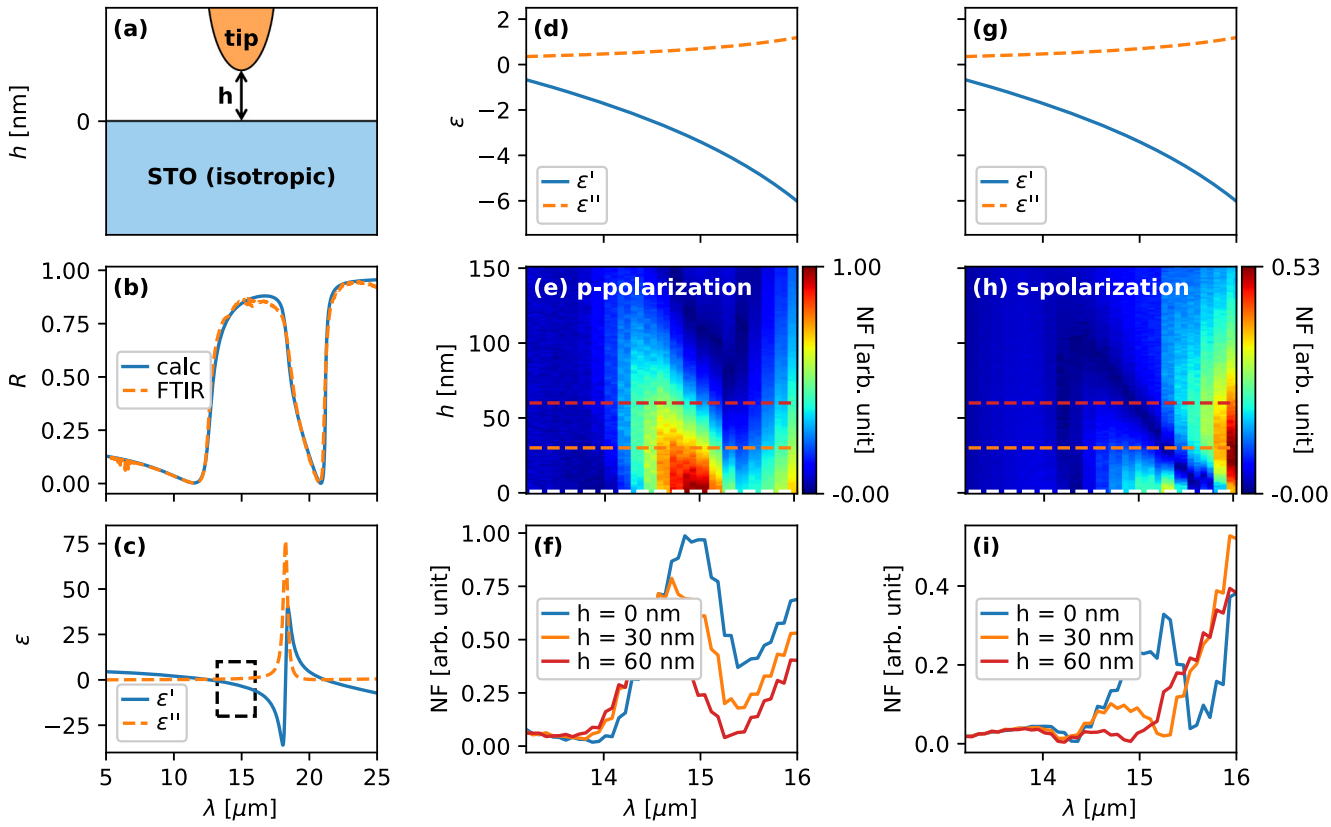

FIG. 2. Far- and near-field response of strontium titanate (STO): (a) Sketch of the experimental near-field setup. (b) Measured far-field reflectance R [35] in comparison to literature data [87]. (c), (d), (g) Overview and detailed view of real and imaginary parts of the permittivity ϵ' and ϵ'', calculated using literature data [87]. The wavelength regime from 13.2–16.0 μm in (d)–(i) is marked with a box in (c). (e), (f), (h), (i) Near-field signal NF measured for different tip-sample distances h and wavelengths λ; in (e) and (f) the illuminating light is p polarized, in (h) and (i) it is s polarized. (f), (i) Spectra for tip-sample distances of $h = 0$, 30, and 60 nm corresponding to the dashed lines in (e) and (h). For clear comparison with theory, the figure is arranged according to Fig. 1. As expected, STO shows an enhanced near-field signal within the reststrahlenband around $\lambda \approx 15$ μm.

respect to the optical axis [90]. We use a commercial sample (YCC, Yamaju Ceramics Co., LTD, Japan) with a surface plane perpendicular to the optical axis [z-cut, (001) surface]. For a far-field reflection measurement at normal incidence [Fig. 3(b)], hence, only the polarization perpendicular to the optical axis needs to be taken into account. For this polarization, corresponding to the ordinary ray, LNO's highest-energy phonon mode occurs at $\lambda_{\mathrm{TO},o} = 17.1$ μm (i.e., 586 cm^{-1} or 17.6 THz, with $\gamma_{\mathrm{TO},o} = 35$ cm^{-1}), its LO mode at $\lambda_{\mathrm{LO},o} = 11.4$ μm (i.e., 878 cm^{-1} or 26.3 THz, with $\gamma_{\mathrm{LO},o} = 15$ cm^{-1}), and $\epsilon_{\infty,o} = 5.0$ [90]. The reflectivity calculated from literature data well matches the measured far-field spectra.

For a polarization parallel to the optical axis (x-cut, extraordinary ray), LNO's highest-energy TO mode occurs at $\lambda_{\mathrm{TO},eo} = 15.9$ μm (i.e., 628 cm^{-1} or 18.8 THz with $\gamma_{\mathrm{TO},eo} = 34$ cm^{-1}), its LO mode at $\lambda_{\mathrm{LO},eo} = 11.5$ μm (i.e., 869 cm^{-1} or 26.1 THz with $\gamma_{\mathrm{LO},eo} = 17$ cm^{-1}), and $\epsilon_{\infty,eo} = 4.6$ [90]. Please note that also a lower-energy phonon mode contributes to the overall optical behavior in the wavelength regime measured here [90]. In Figs. 3(c), 3(d), and 3(g), the calculated permittivity is shown for both polarizations, either parallel to the optical axis ϵ_{eo} or perpendicular to the optical axis ϵ_o. For near-field measurements, generally, the anisotropy of a sample needs to be taken into account. As a first approximation one may use an effective permittivity $\epsilon_{\mathrm{eff}} = \sqrt{\epsilon_{eo}\epsilon_o}$ in order to describe the near-field response [24,30,91], which is why both ϵ_{eo} and ϵ_o are shown here.

For p-polarized incident light [Figs. 3(e) and 3(f)] and $h = 0$, two local maxima in the near-field response are observed with $\lambda_{\mathrm{max},p,1} \approx (13.0 \pm 0.1)$ μm (i.e., 719 cm^{-1} or 21.6 THz), corresponding to $\epsilon'_{\mathrm{eff}} \approx -3.0 \pm 0.3$, and $\lambda_{\mathrm{max},p,2} \approx (13.9 \pm 0.1)$ μm (i.e., 719 cm^{-1} or 21.6 THz), corresponding to $\epsilon'_{\mathrm{eff}} \approx -6.2 \pm 0.6$. For s-polarized incident light [Figs. 3(h) and 3(i)] and $h = 0$, a maximum near-field response is found at $\lambda_{\mathrm{max},s} \approx (13.6 \pm 0.1)$ μm (i.e., 735 cm^{-1} or 22.0 THz), corresponding to $\epsilon'_{\mathrm{eff}} \approx -4.9 \pm 0.5$, i.e., slightly red-shifted in comparison to $\lambda_{\mathrm{max},p,1}$. For increasing tip-sample distance the near-field resonances for both p- and s-polarized incident light shift toward smaller wavelengths, again yielding the characteristic lobe shape. The maximum intensity observed for s polarization is approximately 0.43 times the maximum intensity for p polarization. Yet, similar to STO, the resonance for s polarization appears to continue for $\lambda >$ 14.5 μm, i.e., outside the wavelength range acquired here.

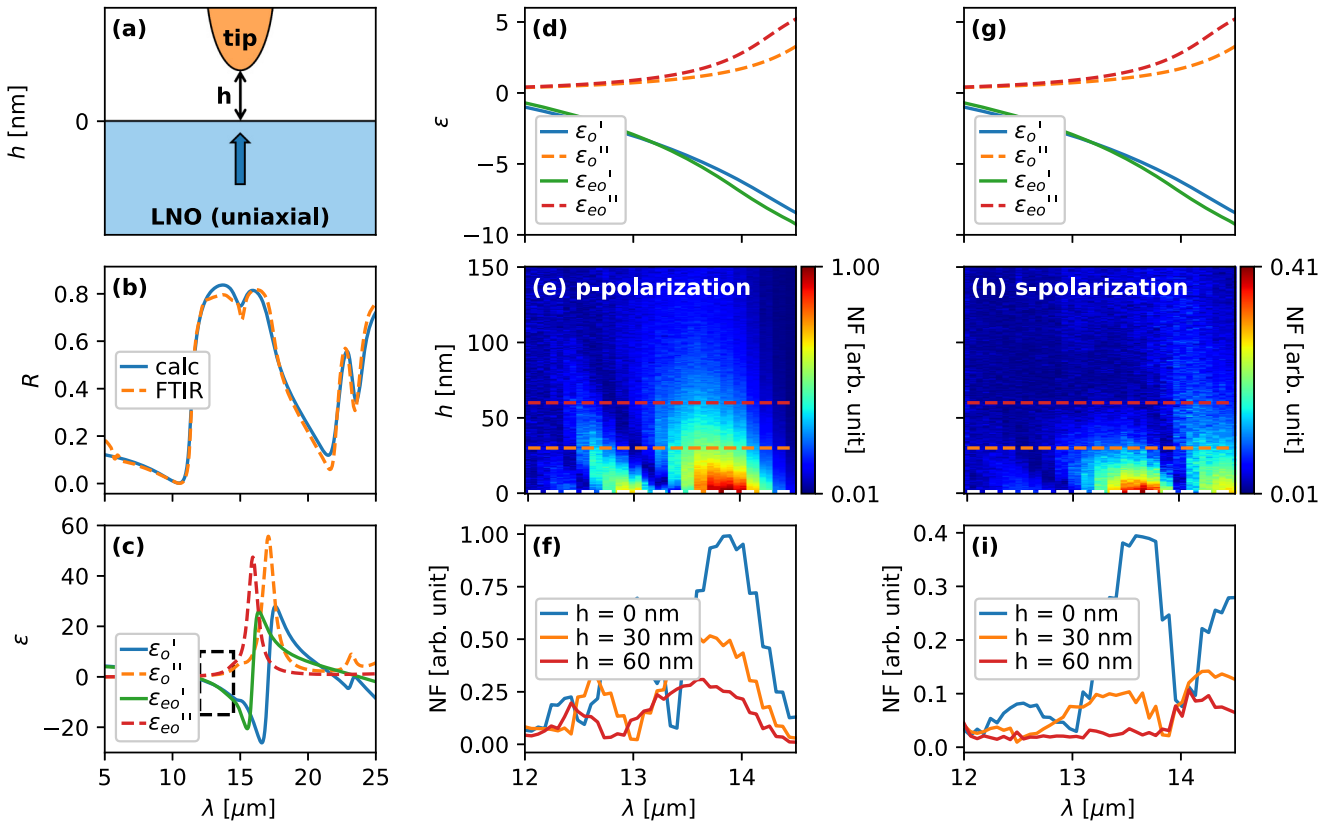

FIG. 3. Far- and near-field responses of lithium niobate (LNO): (a) Sketch of the experimental near-field setup. (b) Measured far-field reflectance R in comparison to literature data [90]. (c), (d), (g) Overview and detailed view of real and imaginary parts of the permittivity ϵ' and ϵ'', calculated using literature data [90]. The wavelength regime from 12.0–14.5 μm in (d)–(i) is marked with a box in (c). (e), (f), (h), (i) Near-field signal NF measured for different tip-sample distances h and wavelengths λ; in (e) and (f) the illuminating light is p polarized, in (h) and (i) it is s polarized. (f), (i) Spectra for tip-sample distances of $h = 0$, 30, and 60 nm corresponding to the dashed lines in (e) and (h). For LNO, the near-field resonance occurs around 12.5–14.5 μm.

3. Lead zirconate titanate (PZT, Zr:Ti = 20:80) thin films

While, hitherto, we discussed two bulk samples, here, we study now a 200-nm-thick tetragonal (001) PZT thin film. According to literature [83], PZT's highest-energy phonon mode occurs at $\lambda_{TO} = 18.1$ μm (i.e., 551 cm^{-1} or 16.5 THz, with $\gamma_{TO} = 37$ cm^{-1}), its LO mode at $\lambda_{LO} = 14.4$ μm (i.e., 695 cm^{-1} or 20.8 THz, with $\gamma_{LO} = 71$ cm^{-1}), and $\epsilon_\infty = 5.2$. Please note that those phonon data were acquired on a PZT thin film grown on a platinized silicon wafer via sol-gel process [83]. The PZT thin film used here, on the other hand, was grown epitaxially by pulsed laser deposition on a (001) STO substrate, which leads to higher crystallinity [83,93]. Due to the diffraction-limited resolution of FTIR and the polycrystalline structure of the literature PZT film [83], values derived from the phonon data are averaged over different orientations of the dielectric tensor. This results in the effective permittivity shown in Figs. 4(c), 4(d), and 4(g) that, as an approximation, is the property relevant for the interpretation of the near-field spectra (refer to previous Sec. III A 2 and Refs. [24,30,91]). The PZT film measured here is 200-nm thick, which at $\lambda \approx 15$ μm corresponds to $\lambda/75$. Hence, the far-field measurement [Fig. 4(b)] is dominated by the STO substrate [compare Fig. 2(b)]. However, taking into account the reflection at the substrate as well as multiple reflections within the thin film [94,95], the resulting calculated reflectivity matches well to the experimental FTIR data [Fig. 4(b)].

In contrast to far-field examinations, near-field measurements typically probe the sample volume up to a depth of about 100 nm [33,96,97], resulting in negligible contributions of the STO substrate to the near-field signal of our 200-nm-thin PZT.[1] The near-field spectra of Figs. 4(e), 4(f), 4(h), and 4(i), indeed, show a signature clearly distinct from STO [Figs. 2(e), 2(f), 2(h), and 2(i)]: For p polarization on PZT, a local maximum in the near-field response is observed at $\lambda_{\max,p,1} \approx (15.3 \pm 0.1)$ μm (i.e., 654 cm^{-1} or 19.6 THz), corresponding to $\epsilon' \approx -1.3 \pm 0.3$; a second maximum occurs at the long-wavelength limit of the range measured here, i.e., $\lambda_{\max,p,2} \geqslant 16.2$ μm (i.e., 617 cm^{-1} or 18.5 THz), corresponding to $\epsilon' \leqslant -3.5 \pm 0.4$. For s polarization, the maximum is observed at $\lambda_{\max,s} \approx (15.8 \pm 0.1)$ μm (i.e., 633 cm^{-1} or

[1] Although not applied in this study, please note that, in principle, the probing volume of s-SNOM might be expanded to interesting nanostructures and features that might be buried even deeper below the sample surface, for instance when utilizing resonant interaction, e.g., superlenses [35,38,109] and/or enhancing layers [110].

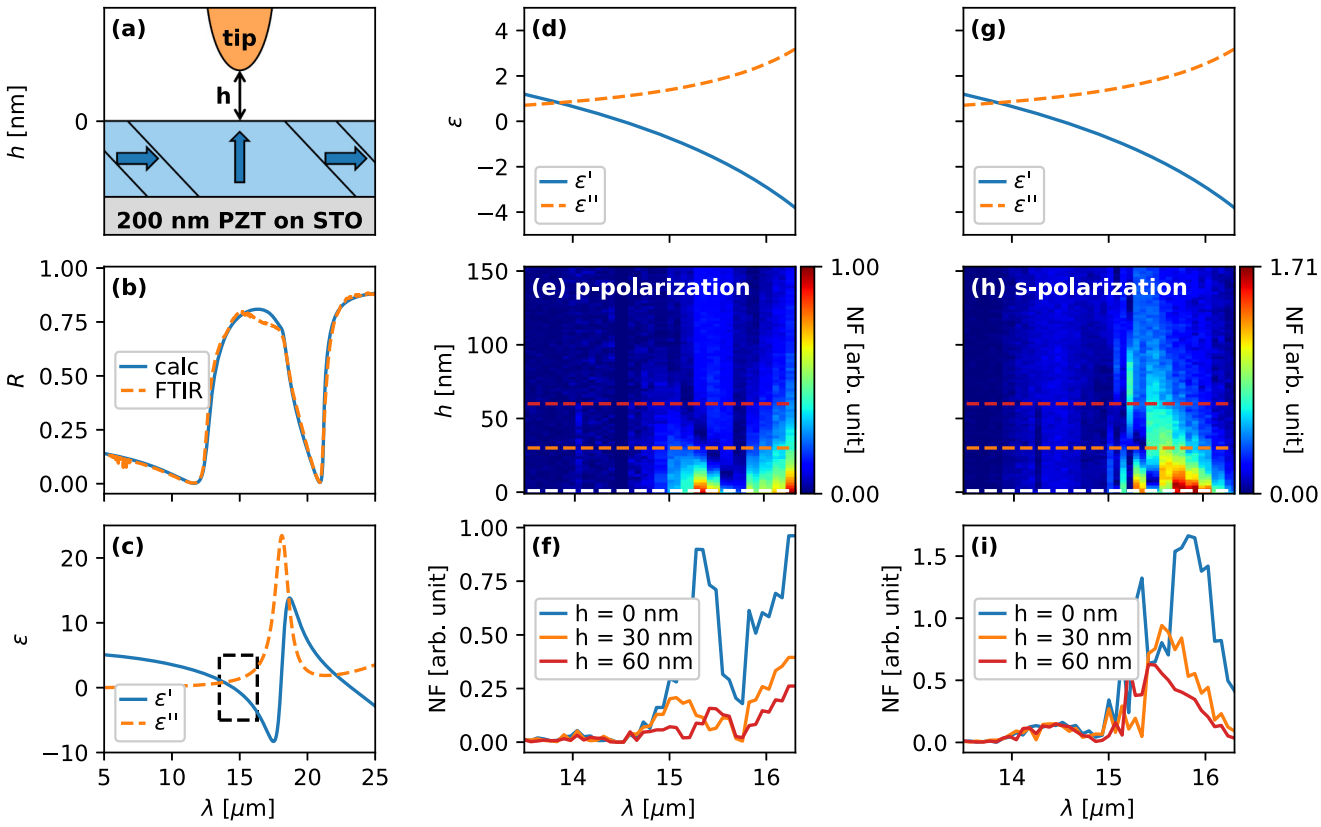

FIG. 4. Far- and near-field responses of lead zirconate titanate (PZT): (a) Sketch of the experimental near-field setup. (b) Measured far-field reflectance R in comparison to thin-film reflectance calculated using phonon data of PZT [83] and STO (substrate) [90] with ϵ_∞ of PZT taken from Ref. [92]. (c), (d), (g) Overview and detailed view of real and imaginary parts of the permittivity, ϵ' and ϵ'', calculated using literature data [83,92]. The wavelength regime from 13.5–16.3 μm in (d)–(i) is marked with a box in (c). (e), (f), (h), (i) Near-field signal NF measured for different tip-sample distances h and wavelengths λ; in (e) and (f) the illuminating light is p polarized, in (h) and (i) it is s polarized. (f), (i) Spectra for tip-sample distances of h = 0, 30, and 60 nm corresponding to the dashed lines in (e) and (h). For PZT, the near-field resonance occurs around 15.0–16.5 μm.

19.0 THz), corresponding to $\epsilon' \approx -2.4 \pm 0.3$. Interestingly, here the maximum response observed for s polarization is about 1.7 times stronger than for p polarization. However, this may be explained by the limited wavelength range of the measurement. Please note that for PZT the general lobelike shape of the near-field resonance appears less distinct as compared to both STO and LNO. This difference may be attributed to the dispersion of PZT in this wavelength regime: In comparison to STO and LNO, the highest-energy phonon mode in PZT is weaker, which leads to a lower variation in permittivity. Moreover, for a given negative real part of the permittivity, absorption is stronger, which significantly reduces the characteristic lobelike shape of the near-field resonance.

B. Imaging ferroelectric domain structures via resonant s-SNOM

We exploit the high spatial resolution of resonant near-field microscopy by studying a 400-nm-thick teragonal (001) PZT thin film grown by pulsed laser deposition on 200-nm-thick (001) $BiFeO_3$ on (100) STO substrate. It shows ferroelectric domains with either in-plane polarization (a domains) or out-of-plane polarization (c domains). Via out-of-plane (oop) piezoresponse force microscopy (PFM) [98–100], the characteristically narrow [101], piezoelectrically inactive a domains can easily be distinguished from the larger c domains that show high oop PFM amplitude [Fig. 5(b)].

While PFM probes the piezoelectric properties of a sample [98–100], s-SNOM is sensitive to the dielectric tensor, i.e., a complementary sample property. In ferroelectrics, generally, the piezoelectric and dielectric tensors are coupled via the unit-cell distortion of the crystal, which gives rise to the formation of both a remanent dielectric polarization and an optical anisotropy axis. For resonant excitation, the s-SNOM's sensitivity on the sample properties is enhanced and a rotation of the dielectric tensor may be probed [24,91]. Particularly, the optical axes of a and c domains are orthogonal for PZT, resulting in a spectral shift of the corresponding near-field resonances of ~0.1 μm [25,26]. Hence, a s-SNOM contrast between the two domain types is expected that must characteristically change its sign when tuning the wavelength between c- and a-domain phonon resonances. Please note that, in contrast to most artificial structures, our sample provides pure dielectric contrast as the ferroelectric domain structure [Figs. 5(b)–5(d)] is decoupled from the surface topography [Fig. 5(a)].

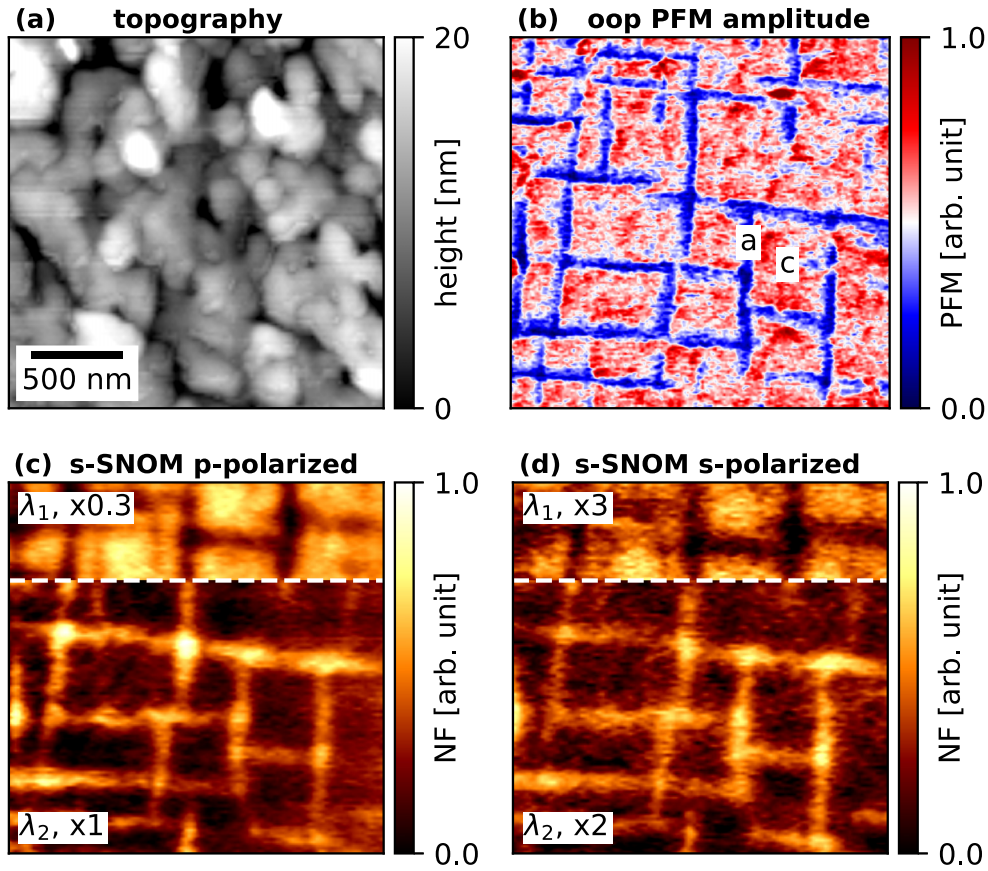

FIG. 5. Ferroelectric domain structure of PZT thin film obtained via complementary methods: (b) Out-of-plane (oop) PFM amplitude map showing high/low response for c/a domains, respectively. The same domain structure is observable in both the *p*- (c) and *s*-polarized (d) near-field images. When changing the wavelength from $\lambda_1 = 15.3\ \mu$m (top quarter) to $\lambda_2 = 15.8\ \mu$m (lower three quarters), the domain contrast is characteristically reversed for both polarizations. In order to enable usage of the same color scale, the obtained signals are multiplied by a constant factor shown in the white boxes. The domain structure shown in (b)–(d) is evidently decoupled from the topography (a), which was measured simultaneously to (d). (a)–(d) Depict the same sample area; scale bar in (a).

In Figs. 5(c) and 5(d), near-field images for *p*- and *s*-polarized incident light are shown, both clearly yielding the ferroelectric domain structure. The top parts of Figs. 5(c) and 5(d) show a near-field excitation at $\lambda_1 = 15.3\ \mu$m, i.e., under resonant conditions for the *c* domains, which consequently appear bright. When the illuminating wavelength is increased to $\lambda_2 = 15.8\ \mu$m [lower parts of Figs. 5(c) and 5(d)] the domain contrast inverts, showing resonantly excited, bright *a* domains [24–26]. Remarkably, the ferroelectric domain pattern is fully probed by near-field microscopy in both polarizations even including the narrow *a* domains. Thinner domains appear less bright whereas cross sections between domains show an enhanced response, indicating that the probing volume is slightly larger than the *a*-domain width. Comparing with the PFM examination, we were able to determine the lateral resolution of our technique to be in the order of ∼10 nm for both polarizations used. The power-normalized signal strength is in the same order of magnitude at both wavelengths and for both polarizations. Highest near-field signals and contrasts, however, are observed for *p*-polarized incident light at the shorter wavelength λ_1 for which the absorption of the material is lowest and the long axis of the tip yields highest field enhancement.

IV. DISCUSSION AND SUMMARY

Resonant s-SNOM enables a highly material-specific response at mid-infrared wavelengths. We provide spectroscopic measurements of the phonon-induced near-field resonances of STO, LNO, and PZT for both *p*- and *s*-polarized incident light. Thereby, we can experimentally confirm that resonant near-field spectroscopy is, indeed, possible for orthogonal incident polarizations. Especially, *s*-polarized incident light also yields a strong near-field enhancement of the same order of magnitude as for the *p*-polarized case.

We apply the analytical dipole model for qualitative description of the near-field resonance since it allows predictions for polarizations both perpendicular and parallel to the sample surface. Please note that the dipole model here is not meant to fully represent the physical interaction scenario between tip and sample, particularly concerning reflection at the sample surface, rotation of polarization due to oblique illumination, as well as specific shape and inclination angle of the tip. Yet, it is a highly suitable model to discuss the principal behavior of near-field coupled systems. In literature, comparisons of the dipole model and experimental observation are discussed for *p*-polarized field components only

TABLE I. Important wavelengths of the phonon-induced material response: LO and TO phonon mode (via FTIR measurement) and near-field resonances (for both *p* and *s* polarization, i.e., *p*-/*s*-pol NF). For LNO, LO and TO modes depend on the polarization [ordinary (*o*) and extraordinary (*eo*)]. The permittivity ϵ corresponding to the near-field resonances (ϵ_{res}) put in brackets after each wavelength. If multiple NF maxima exist, the maximum at smallest wavelength was chosen (see Sec. III A).

Material	LO mode (μm)	TO mode (μm)	*p*-pol NF (μm) (ϵ_{res})	*s*-pol NF (μm) (ϵ_{res})
$SrTiO_3$	12.6 [87]	18.2 [87]	14.9 ($-3.2+0.7i$)	15.3 ($-4.1+0.8i$)
$LiNbO_3$	11.4 (*o*) [90] 11.5 (*eo*) [90]	17.1 (*o*) [90] 15.9 (*eo*) [90]	13.0 ($-3.0+0.8i$)	13.6 ($-4.9+1.4i$)
$PbZr_{0.2}Ti_{0.8}O_3$	14.4 [83]	18.1 [83]	15.3 ($-1.3+1.6i$)	15.8 ($-2.4+2.2i$)

[11,28,30,75,76,78,80,82,84]. Our report here is a comparison between dipole model and experiment for *s*-polarized components at resonant excitation, including spectral position and distance dependence of the near-field response.

For *p* polarization, the spectral positions of the first near-field resonance lobes of STO, LNO, and PZT correspond to real parts of the permittivity ϵ' of -3.2, -3.0, and -1.3, respectively (Table I), which matches the dipole model's prediction with the first resonance lobe at $\epsilon' \approx -2.6$ for *p*-polarized field components. For *s*-polarized field components, the dipole model predicts a blue-shift of the near-field resonance with respect to *p*-polarized orientation. In contrast, especially for the bulk samples, STO and LNO, our experimental observations show a red-shift (Table I), which might be explained by a reduced effective distance between tip-dipole and sample surface or higher-order multipoles [80] that were not considered in our simple dipolar approximation.

Nevertheless, the characteristic lobelike shape for the near-field response plotted as a function of wavelength and tip-sample distance, predicted by the dipole model for both polarizations, is clearly confirmed by our experiments. Especially, the blue-shift of the resonance with increasing tip-sample distance [24,30,84] is evident (see Figs. 2–4).

An important advantage of near-field techniques is the strong confinement of the probing volume in both vertical and lateral direction. The former allows for the characterization of thin films with negligible influence of the substrate. The latter results in a high lateral resolution in the order of $\sim$10 nm, which we confirm for different polarizations via resonant near-field imaging of the ferroelectric domain structure of PZT.

In conclusion, using both *p*- and *s*-polarized mid-infrared incident light, we obtain insight to phonon-induced near-field resonances both regarding polarization dependence and material range. Our study demonstrates the general applicability of polarization-dependent resonant near-field spectroscopy and microscopy and thereby opens a field for further detailed analysis and development. We think that our results will be of special benefit to infrared material analysis at the nanoscale, there paving the way for new approaches, e.g., to the analysis of anisotropic materials, and directly serving as reference spectra. Moreover, for the example of a PZT thin film, we demonstrate the strong confinement of the probing volume in both vertical and lateral directions, allowing for thin-film characterization without substrate influences and optical imaging of ferroelectric domain structure far below the diffraction limit.

ACKNOWLEDGMENTS

We thank P. Shafer, P. Yu, and R. Ramesh for providing the PZT thin-film samples, as well as M. Fehrenbacher for FTIR characterization of the LNO sample, and J. Döring for support with the SNOM measurements. We are grateful to P. Michel, J. M. Klopf, and the FELBE team at Helmholtz-Zentrum Dresden-Rossendorf for their dedicated support. Moreover, we thank the Helmholtz-Zentrum Dresden-Rossendorf for providing laboratory space, technical assistance, and the required cryogenics. This project has been funded by the DFG under Grant No. KE2068/2-1 and by the BMBF under Grant No. 05K16ODA as well as by the German Academic Exchange Service DAAD and the Würzburg-Dresden Cluster of Excellence on Complexity and Topology in Quantum Matter (ct.qmat). X.Z. acknowledges the funding support from the Gordon and Betty Moore Foundation and the Office of Naval Research (ONR) MURI program under Grant No. N00014-13-1-0631.

S.C.K. conceptualized this study, Y.L., S.C.K., and X.Z. characterized the STO sample and the PZT thin films via FTIR, L.W., D.L., and S.C.K. performed the SNOM measurements, S.C.K. carried out the PFM measurements, L.W. and S.C.K. analyzed the experimental results and performed the calculations with the dipole model, L.W., L.M.E., and S.C.K. wrote the draft, with all authors contributing to the manuscript.

APPENDIX A: INTRODUCTION TO THE DIPOLE MODEL

Within the dipole model, the tip-sample system is approximated via an induced point dipole within the tip and its mirror dipole within the sample. These dipoles couple via dipole-dipole interaction, leading to an effective polarizability of the system α_{eff} [74]. The field scattered off the combined tip-sample system E_{sca} may be written as [102–104]

$$\vec{E}_{\mathrm{sca}} \propto \hat{\alpha}_{\mathrm{eff}} \vec{E}_{\mathrm{inc}}.$$

In general, both the incoming electric field E_{inc} and the field scattered at the tip will be reflected at the sample surface [76]. However, following the most widely used description of the dipole model [16,28,29,74,102–104], we will neglect reflection on the sample in the following. The effective polarizability depends on the incoming polarization and can be written for *p*- and *s*-polarized components as

$$\alpha_{\mathrm{eff},p} = \frac{\alpha(1+\beta)}{1-\frac{\alpha\beta}{16\pi(z)^3}} \text{ and } \alpha_{\mathrm{eff},s} = \frac{\alpha(1-\beta)}{1-\frac{\alpha\beta}{32\pi(z)^3}},$$

respectively, $\alpha \approx 4\pi a^3$ is the polarizability of a metallic spherical tip, assumed to be constant in the relevant wavelength regime, a is the tip radius, z is the distance between tip and sample, and $\beta = (\epsilon - 1)/(\epsilon + 1)$ is the sample response function with $\epsilon = \epsilon(\lambda)$ being the wavelength-dependent complex permittivity of the sample [74,80]. The tip-sample distance z is assumed to vary sinusoidally due to the cantilever oscillation: $z = h + f_{num}a + A[1 + \sin(\omega t)]$. We set the oscillation amplitude $A = 40$ nm, vary h according to the values shown in Fig. 1 and set ω to 1 as it is an arbitrary parameter for our simulation. The factor f_{num} accounts for numerical calculations [80] and experimental observations [30] showing that the effective tip dipole is shifted toward the sample within the tip [30,80]. Here, $f_{num} = 0.785$ in accordance to literature for p polarization [80]. For a higher accuracy of the description, it may be useful to assume polarization-dependent $f_{num} = f_{num,p/s}$, which will require additional numerical calculations that are beyond the scope of this paper. When the dipole model is used to describe near-field interaction, usually an effective tip radius larger than the physical tip radius is chosen [30,75]. We set $a = 600$ nm, which equals values found in literature, like the effective tip length in Ref. [76] (finite-dipole model) or the effective tip radius in Ref. [30] (dipole model).

In our experimental setup we apply a self-homodyne detection scheme and higher-harmonic demodulation [74]: At the detector, the signal E_{sca} interferes with background scattering E_{bg} by the probe shaft and the sample, which leads to the detection of $|E_{\mathrm{sca}} + E_{bg}|^2 = |E_{\mathrm{sca}}|^2 + |E_{bg}|^2 + 2|E_{\mathrm{sca}}||E_{bg}|\cos(\varphi_{\mathrm{sca}} - \phi_{bg})$. Here, usually $|E_{bg}|^2 \gg 2|E_{\mathrm{sca}}||E_{bg}|\cos(\phi_{\mathrm{sca}} - \phi_{bg}) \gg |E_{\mathrm{sca}}|^2$. The background scattering $|E_{bg}|^2$ is assumed to vary no more than linearly with tip-sample distance [74]. Therefore, demodulation at at higher-harmonic frequencies $n\omega$ with $n \geqslant 2$ effectively suppresses the background term [74]. In conclusion, the demodulated near-field response will be dominated by $2|E_{\mathrm{sca}}||E_{bg}|\cos(\phi_{\mathrm{sca}} - \phi_{bg})$. For the sake of simplicity, we set $|E_{bg}| = 1$ and assume $\phi_{bg} = 0$ in our theoretical analysis. However, note that, generally, both $|E_{bg}|$ and ϕ_{bg} might depend on experimental parameters and, e.g., not be constant for varying wavelength. Yet, a more detailed analysis is beyond the scope of this paper. Assuming constant E_{bg}, the expected near-field signal reduces to $|E_{\mathrm{sca}}|\cos(\phi_{\mathrm{sca}}) = \mathrm{Re}(E_{\mathrm{sca}})$. In the experiment (Appendix B), higher-harmonic demodulation is applied, with the nth harmonic of the near-field signal corresponding to the signal contribution at $n\omega$. In our theoretical approach, we represent this step by applying a fast Fourier transformation to $\mathrm{Re}(E_{\mathrm{sca}})$ and taking the absolute of its value at $n\omega$. Here, we chose $n = 2$ as an estimate for our expected near-field signal (Fig. 1), which corresponds to the experimental situation.

APPENDIX B: EXPERIMENTAL SETUP

The far-field FTIR spectra were obtained with the commercial instruments "Bruker Vertex 80v" (for the LNO sample) and "Bruker IFS 125HR" (for the STO and PZT samples) with unpolarized light. The measurement on LNO was performed with a weakly focused beam (N.A.= 0.1) at an incident angle of about 10° with reference to the sample normal and referenced to the reflectivity of a gold mirror. The STO and PZT spectra were obtained with two different settings, depending on the spectral regime: For $\lambda = 5.0$ to 15.9 μm (region 1), incident light has been focused (N.A. = 0.5, microscope unit of the Bruker IFS 125HR) at an incident angle of 0° whereas for $\lambda = 15.2$ to 25.0 μm (region 2), a weakly focused beam at an incident angle of about 10° has been utilized. For both spectral regimes a silver mirror has been used as reference. Spectral resolution ranges from 0.5 to 2.0 cm^{-1} corresponding to 20 to 80 nm at the position of the phonon modes around 20 μm. The resulting reflectivity of both STO [35] and PZT each were multiplied with an adapted factor for comparison to the calculations based on literature phonon data. For STO and PZT, respectively, this factor was set to 0.850, and 0.805 for region 1, and 1.035 and 0.845 for region 2. This scaling factor compensates for incident angle variations and imperfect reflectivity of the reference mirrors as well as minor variations in the experimental alignment (sample exchange). For LNO, the resulting reflectivity is displayed without applying any further corrections. Piezoresponse force microscopy was performed on a commercial "Multimode Nanoscope" AFM by Digital Instruments.

For the near-field investigations we use a home-built s-SNOM [19,24,30,35,38,105,106]: we implement a self-homodyne detection scheme [74] in combination with higher-harmonic demodulation [28,74,107] to distinguish the desired near-field response from far-field contributions. Spectroscopic near-field data shown in this publication are demodulated at the second harmonic of the cantilever's frequency ($n = 2$); image data shown in Sec. III B are demodulated at the third harmonic ($n = 3$). We use a platinum-iridium coated silicon cantilever, which is driven at its eigenfrequency (≈ 160 kHz) with an amplitude of $A \approx 40$ nm. Our cantilever is mounted with an inclination of about 15° with respect to the sample surface, which may lead to an increased sensitivity for s-polarized measurements in comparison to strictly horizontal alignment [53]. For illumination of our SNOM-tip, we use the narrow-band free-electron laser FELBE at Helmholtz-Zentrum Dresden-Rossendorf, Germany [19,24–27,30,35,38,105,106]. It is a tunable, linearly polarized laser source with a repetition rate of 13 MHz (quasicontinuous mode), which covers the infrared wavelength regime from 5–250 μm, i.e., 40–2000 cm^{-1} or 1.2–60.0 THz. The direction of polarization is changed from "s" to "p polarization", i.e., electric field components parallel and perpendicular to the optical table, via periscope optics. The light is focused onto the tip via a parabolic mirror at an angle of 70° with respect to the sample normal. The direction of polarization will be turned due to reflection at the parabolic mirror at oblique angle. Hence, p and s polarization will not be identical to theory Sec. II. Yet, after reflection at the parabolic mirror the two polarizations will remain orthogonal. For detection of the backscattered light, we use mercury cadmium telluride detectors with different cutoff wavelengths depending on the wavelength regime investigated. As ferroelectric materials are also pyroelectric, illumination with an infrared light source leads to charging of the sample. In order to obtain unbiased

near-field contrast, the voltage difference between tip and sample is nullified by operating a Kelvin control loop (KPFM) [24,27,108].

In this publication, we present near-field data as a function of both wavelength λ and tip-sample distance h. The data were obtained as follows: The FEL is tuned to the starting wavelength and used to illuminate the s-SNOM tip. The tip is then put into feedback and, after several seconds for stabilization, a so-called retract curve is started, where the tip-sample distance is monotonously increased up to a certain maximum distance of a few 100 nm while measuring the evolution of the near-field response. For the spectroscopic response, retract curves are repeated for every wavelength; the FEL wavelength is tuned by changing the undulator gap width at a fixed electron energy. The near-field images in Figs. 5(c) and 5(d) were obtained by scanning the sample while keeping the tip at a fixed position; background plane subtraction was applied for better contrast visualization. All near-field data shown here are normalized to the incident laser power, which is measured simultaneously.

[1] S. Amarie, P. Zaslansky, Y. Kajihara, E. Griesshaber, W. W. Schmahl, and F. Keilmann, Beilstein J. Nanotechnol. **3**, 312 (2012).

[2] R. Esteban, R. Vogelgesang, J. Dorfmüller, A. Dmitriev, C. Rockstuhl, C. Etrich, and K. Kern, Nano Lett. **8**, 3155 (2008).

[3] P. Alonso-González, P. Albella, M. Schnell, J. Chen, F. Huth, A. García-Etxarri, F. Casanova, F. Golmar, L. Arzubiaga, L. E. Hueso, J. Aizpurua, and R. Hillenbrand, Nat. Commun. **3**, 684 (2012).

[4] B. Stuart, *Modern Infrared Spectroscopy* (Wiley, Chichester, 1996).

[5] R. M. Stöckle, Y. D. Suh, V. Deckert, and R. Zenobi, Chem. Phys. Lett. **318**, 131 (2000).

[6] P. Hermann, H. Fabian, D. Naumann, and A. Hermelink, J. Phys. Chem. C **115**, 24512 (2011).

[7] M. Specht, J. D. Pedarnig, W. M. Heckl, and T. W. Hänsch, Phys. Rev. Lett. **68**, 476 (1992).

[8] Y. Inouye and S. Kawata, Opt. Lett. **19**, 159 (1994).

[9] F. Zenhausern, M. P. O'Boyle, and H. K. Wickramasinghe, Appl. Phys. Lett. **65**, 1623 (1994).

[10] A. Lahrech, R. Bachelot, P. Gleyzes, and A. C. Boccara, Opt. Lett. **21**, 1315 (1996).

[11] S. Amarie and F. Keilmann, Phys. Rev. B **83**, 045404 (2011).

[12] M. von Ardenne, Z. Phys. **109**, 553 (1938).

[13] S. W. Hell and J. Wichmann, Opt. Lett. **19**, 780 (1994).

[14] E. Betzig, G. H. Patterson, R. Sougrat, O. W. Lindwasser, S. Olenych, J. S. Bonifacino, M. W. Davidson, J. Lippincott-Schwartz, and H. F. Hess, Science **313**, 1642 (2006).

[15] M. J. Rust, M. Bates, and X. Zhuang, Nat. Methods **3**, 793 (2006).

[16] B. Knoll and F. Keilmann, Nature (London) **399**, 134 (1999).

[17] T. Taubner, R. Hillenbrand, and F. Keilmann, J. Microsc. **210**, 311 (2003).

[18] A. J. Huber, F. Keilmann, J. Wittborn, J. Aizpurua, and R. Hillenbrand, Nano Lett. **8**, 3766 (2008).

[19] F. Kuschewski, H.-G. von Ribbeck, J. Döring, S. Winnerl, L. M. Eng, and S. C. Kehr, Appl. Phys. Lett. **108**, 113102 (2016).

[20] M. P. Nikiforov, S. C. Kehr, T.-H. Park, P. Milde, U. Zerweck, C. Loppacher, L. M. Eng, M. J. Therien, N. Engheta, and D. Bonnell, J. Appl. Phys. **106**, 114307 (2009).

[21] M. Brehm, T. Taubner, R. Hillenbrand, and F. Keilmann, Nano Lett. **6**, 1307 (2006).

[22] I. Amenabar, S. Poly, W. Nuansing, E. H. Hubrich, A. A. Govyadinov, F. Huth, R. Krutokhvostov, L. Zhang, M. Knez, J. Heberle, A. M. Bittner, and R. Hillenbrand, Nat. Commun. **4**, 2890 (2013),

[23] C. Liewald, S. Mastel, J. Hesler, A. J. Huber, R. Hillenbrand, and F. Keilmann, Optica **5**, 159 (2018).

[24] S. C. Kehr, M. Cebula, O. Mieth, T. Härtling, J. Seidel, S. Grafström, L. M. Eng, S. Winnerl, D. Stehr, and M. Helm, Phys. Rev. Lett. **100**, 256403 (2008).

[25] J. Döring, H.-G. von Ribbeck, M. Fehrenbacher, S. C. Kehr, and L. M. Eng, Appl. Phys. Lett. **105**, 053109 (2014).

[26] J. Döring, D. Lang, L. Wehmeier, F. Kuschewski, T. Nörenberg, S. C. Kehr, and L. M. Eng, Nanoscale **10**, 18074 (2018).

[27] D. Lang, J. Döring, T. Nörenberg, Á. Butykai, I. Kézsmárki, H. Schneider, S. Winnerl, M. Helm, S. C. Kehr, and L. M. Eng, Rev. Sci. Instrum. **89**, 033702 (2018).

[28] R. Hillenbrand, T. Taubner, and F. Keilmann, Nature (London) **418**, 159 (2002).

[29] F. Keilmann and R. Hillenbrand, Philos. Trans.: Math., Phys. Eng. Sci. **362**, 787 (2004).

[30] S. C. Schneider, J. Seidel, S. Grafström, L. M. Eng, S. Winnerl, D. Stehr, and M. Helm, Appl. Phys. Lett. **90**, 143101 (2007).

[31] A. J. Huber, A. Ziegler, T. Köck, and R. Hillenbrand, Nat. Nanotechnol. **4**, 153 (2009).

[32] A. Huber, N. Ocelic, T. Taubner, and R. Hillenbrand, Nano Lett. **6**, 774 (2006).

[33] R. Jacob, S. Winnerl, H. Schneider, M. Helm, M. T. Wenzel, H.-G. von Ribbeck, L. M. Eng, and S. C. Kehr, Opt. Express **18**, 26206 (2010).

[34] M. Lewin, C. Baeumer, F. Gunkel, A. Schwedt, F. Gaussmann, J. Wueppen, P. Meuffels, B. Jungbluth, J. Mayer, R. Dittmann, R. Waser, and T. Taubner, Adv. Funct. Mater. **28** (2018),

[35] S. C. Kehr, Y. M. Liu, L. W. Martin, P. Yu, M. Gajek, S.-Y. Yang, C.-H. Yang, M. T. Wenzel, R. Jacob, H.-G. von Ribbeck, M. Helm, X. Zhang, L. M. Eng, and R. Ramesh, Nat. Commun. **2**, 249 (2011).

[36] C. Long, W. Dong-Li, D. Si-Yuan, Y. Yue-Dong, F. Xiao-Dong, W. Lai-Ming, and Z. Chang-Gan, J. Infrared Millim. W. **36**, 534 (2017).

[37] D. J. Lahneman, T. J. Huffman, P. Xu, S. L. Wang, T. Grogan, and M. M. Qazilbash, Opt. Express **25**, 20421 (2017).

[38] S. C. Kehr, P. Yu, Y. Liu, M. Parzefall, A. I. Khan, R. Jacob, M. T. Wenzel, H.-G. von Ribbeck, M. Helm, X. Zhang, L. M. Eng, and R. Ramesh, Opt. Mater. Express **1**, 1051 (2011).

[39] J. Sun, N. M. Litchinitser, and J. Zhou, ACS Photon. **1**, 293 (2014).

[40] E. Betzig, J. K. Trautman, J. S. Weiner, T. D. Harris, and R. Wolfe, Appl. Opt. **31**, 4563 (1992).

[41] J. A. Porto, R. Carminati, and J.-J. Greffet, J. Appl. Phys. **88**, 4845 (2000).

[42] L. Aigouy, A. Lahrech, S. Grésillon, H. Cory, A. C. Boccara, and J. C. Rivoal, Opt. Lett. **24**, 187 (1999).

[43] Z. H. Kim and S. R. Leone, Opt. Express **16**, 1733 (2008).

[44] D.-S. Kim and Z. H. Kim, Opt. Express **20**, 8689 (2012).

[45] K. I. Kiesow, S. Dhuey, and T. G. Habteyes, Appl. Phys. Lett. **105**, 053105 (2014).

[46] T. G. Habteyes, I. Staude, K. E. Chong, J. Dominguez, M. Decker, A. Miroshnichenko, Y. Kivshar, and I. Brener, ACS Photon. **1**, 794 (2014).

[47] R. L. Olmon, P. M. Krenz, A. C. Jones, G. D. Boreman, and M. B. Raschke, Opt. Express **16**, 20295 (2008).

[48] J. Dorfmüller, R. Vogelgesang, R. T. Weitz, C. Rockstuhl, C. Etrich, T. Pertsch, F. Lederer, and K. Kern, Nano Lett. **9**, 2372 (2009).

[49] A. C. Jones, R. L. Olmon, S. E. Skrabalak, B. J. Wiley, Y. N. Xia, and M. B. Raschke, Nano Lett. **9**, 2553 (2009).

[50] M. Schnell, A. García-Etxarri, A. J. Huber, K. Crozier, J. Aizpurua, and R. Hillenbrand, Nat. Photon. **3**, 287 (2009).

[51] M. Schnell, A. Garcia-Etxarri, A. J. Huber, K. B. Crozier, A. Borisov, J. Aizpurua, and R. Hillenbrand, J. Phys. Chem. C **114**, 7341 (2010).

[52] M. Schnell, A. Garcia-Etxarri, J. Alkorta, J. Aizpurua, and R. Hillenbrand, Nano Lett. **10**, 3524 (2010).

[53] K.-D. Park and M. B. Raschke, Nano Lett. **18**, 2912 (2018).

[54] M. E. Lines and A. M. Glass, *Principles and Applications of Ferroelectrics and Related Materials*, The International Series of Monographs on Physics (Clarendon, Oxford, 1977).

[55] G. Shirane and F. Jona, *Ferroelectric Crystals*, International Series of Monographs on Solid State Physics Vol. 1 (Pergamon, Oxford, 1962).

[56] *Physics of Ferroelectrics: A Modern Perspective*, edited by K. M. Rabe, C. H. Ahn, and J.-M. Triscone, Topics in Applied Physics (Springer, Berlin, 2007).

[57] J. Wang, J. B. Neaton, H. Zheng, V. Nagarajan, S. B. Ogale, B. Liu, D. Viehland, V. Vaithyanathan, D. G. Schlom, U. V. Waghmare, N. A. Spaldin, K. M. Rabe, M. Wuttig, and R. Ramesh, Science **299**, 1719 (2003).

[58] N. A. Hill, J. Phys. Chem. B **104**, 6694 (2000).

[59] A. Sharan, J. Lettieri, Y. Jia, W. Tian, X. Pan, D. G. Schlom, and V. Gopalan, Phys. Rev. B **69**, 214109 (2004).

[60] G. Catalan and J. F. Scott, Adv. Mater. **21**, 2463 (2009).

[61] M. Veithen, X. Gonze, and P. Ghosez, Phys. Rev. Lett. **93**, 187401 (2004).

[62] G. D. Boyd, R. C. Miller, K. Nassau, W. L. Bond, and A. Savage, Appl. Phys. Lett. **5**, 234 (1964).

[63] E. Dagotto, T. Hotta, and A. Moreo, Phys. Rep. **344**, 1 (2001).

[64] R. J. Cava, B. Batlogg, R. B. van Dover, D. W. Murphy, S. Sunshine, T. Siegrist, J. P. Remeika, E. A. Rietman, S. Zahurak, and G. P. Espinosa, Phys. Rev. Lett. **58**, 1676 (1987).

[65] Y. Maeno, H. Hashimoto, K. Yoshida, S. Nishizaki, T. Fujita, J. G. Bednorz, and F. Lichtenberg, Nature (London) **372**, 532 (1994).

[66] D. Panda and T.-Y. Tseng, Ferroelectrics **471**, 23 (2014).

[67] S. D. Stranks and H. J. Snaith, Nat. Nanotechnol. **10**, 391 (2015).

[68] M. A. Green, A. Ho-Baillie, and H. J. Snaith, Nat. Photon. **8**, 506 (2014).

[69] R. G. Batchko, V. Y. Shur, M. M. Fejer, and R. L. Byer, Appl. Phys. Lett. **75**, 1673 (1999).

[70] R. Waser, R. Dittmann, G. Staikov, and K. Szot, Adv. Mater. **21**, 2632 (2009).

[71] A. S. Bhalla, R. Guo, and R. Roy, Mater. Res. Innovations **4**, 3 (2000).

[72] D. G. Schlom, L.-Q. Chen, X. Pan, A. Schmehl, and M. A. Zurbuchen, J. Am. Ceram. Soc. **91**, 2429 (2008).

[73] F. Zenhausern, Y. Martin, and H. K. Wickramasinghe, Science **269**, 1083 (1995).

[74] B. Knoll and F. Keilmann, Opt. Commun. **182**, 321 (2000).

[75] L. Stebounova, B. B. Akhremitchev, and G. C. Walker, Rev. Sci. Instrum. **74**, 3670 (2003).

[76] A. Cvitkovic, N. Ocelic, and R. Hillenbrand, Opt. Express **15**, 8550 (2007).

[77] A. S. McLeod, P. Kelly, M. D. Goldflam, Z. Gainsforth, A. J. Westphal, G. Dominguez, M. H. Thiemens, M. M. Fogler, and D. N. Basov, Phys. Rev. B **90**, 085136 (2014).

[78] H. Wang, L. Wang, D. S. Jakob, and X. G. Xu, Nat. Commun. **9**, 2005 (2018).

[79] J. A. Porto, P. Johansson, S. P. Apell, and T. López-Ríos, Phys. Rev. B **67**, 085409 (2003).

[80] J. Renger, S. Grafström, L. M. Eng, and R. Hillenbrand, Phys. Rev. B **71**, 075410 (2005).

[81] B.-Y. Jiang, L. M. Zhang, A. H. Castro Neto, D. N. Basov, and M. M. Fogler, J. Appl. Phys. **119**, 054305 (2016).

[82] L. Wang and X. G. Xu, Nat. Commun. **6**, 8973 (2015).

[83] T. D. Kang, G. S. Lee, H. S. Lee, H. Lee, Y. S. Kang, S.-J. Cho, B. Xiao, H. Morkoc, and P. G. Snyder, J. Korean Phys. Soc. **49**, 1604 (2006).

[84] T. Taubner, F. Keilmann, and R. Hillenbrand, Nano Lett. **4**, 1669 (2004).

[85] I. E. Kuznetsova, B. D. Zaitsev, S. G. Joshi, and I. A. Borodina, IEEE Trans. Ultrason. Ferroelectr. Freq. Control **48**, 322 (2001).

[86] B. Jaffe, *Piezoelectric Ceramics* (Elsevier, St. Louis, MO, 1971).

[87] J. Petzelt, T. Ostapchuk, I. Gregora, I. Rychetský, S. Hoffmann-Eifert, A. V. Pronin, Y. Yuzyuk, B. P. Gorshunov, S. Kamba, V. Bovtun, J. Pokorný, M. Savinov, V. Porokhonskyy, D. Rafaja, P. Vaněk, A. Almeida, M. R. Chaves, A. A. Volkov, M. Dressel, and R. Waser, Phys. Rev. B **64**, 184111 (2001).

[88] W. G. Spitzer, R. C. Miller, D. A. Kleinman, and L. E. Howarth, Phys. Rev. **126**, 1710 (1962).

[89] S. B. Levin, N. J. Field, F. M. Plock, and L. Merker, J. Opt. Soc. Am. **45**, 737 (1955).

[90] A. S. Barker and R. Loudon, Phys. Rev. **158**, 433 (1967).

[91] S. C. Schneider, S. Grafström, and L. M. Eng, Phys. Rev. B **71**, 115418 (2005).

[92] G. Burns and B. A. Scott, Phys. Rev. Lett. **25**, 167 (1970).

[93] K. S. Hwang, T. Manabe, T. Nagahama, I. Yamaguchi, T. Kumagai, and S. Mizuta, Thin Solid Films **347**, 106 (1999).

[94] M. Born, *Principles of Optics: Electromagnetic Theory of Propagation, Interference and Diffraction of Light*, 7th ed. (Cambridge University Press, Cambridge, 1999).

[95] O. S. Heavens, *Thin Film Physics* (Methuen, London, 1973).

[96] L. Jung, B. Hauer, P. Li, M. Bornhöfft, J. Mayer, and T. Taubner, Opt. Express **24**, 4431 (2016).

[97] T. Taubner, F. Keilmann, and R. Hillenbrand, Opt. Express **13**, 8893 (2005).
[98] P. Güthner and K. Dransfeld, Appl. Phys. Lett. **61**, 1137 (1992).
[99] L. M. Eng, H.-J. Güntherodt, G. A. Schneider, U. Köpke, and J. Muñoz Saldaña, Appl. Phys. Lett. **74**, 233 (1999).
[100] L. M. Eng, Nanotechnology **10**, 405 (1999).
[101] L. Feigl, P. Yudin, I. Stolichnov, T. Sluka, K. Shapovalov, M. Mtebwa, C. S. Sandu, X.-K. Wei, A. K. Tagantsev, and N. Setter, Nat. Commun. **5**, 4677 (2014).
[102] R. Hillenbrand, B. Knoll, and F. Keilmann, J. Microsc. **202**, 77 (2001).
[103] R. Hillenbrand and F. Keilmann, Appl. Phys. B **73**, 239 (2001).
[104] N. Ocelic and R. Hillenbrand, Nat. Mater. **3**, 606 (2004).
[105] S. C. Kehr, R. G. P. McQuaid, L. Ortmann, T. Kämpfe, F. Kuschewski, D. Lang, J. Döring, J. M. Gregg, and L. M. Eng, ACS Photon. **3**, 20 (2016).
[106] S. C. Kehr, J. Döring, M. Gensch, M. Helm, and L. M. Eng, Synch. Radiat. News **30**, 31 (2017).
[107] G. Wurtz, R. Bachelot, and P. Royer, Rev. Sci. Instrum. **69**, 1735 (1998).
[108] U. Zerweck, C. Loppacher, T. Otto, S. Grafström, and L. M. Eng, Phys. Rev. B **71**, 125424 (2005).
[109] T. Taubner, D. Korobkin, Y. Urzhumov, G. Shvets, and R. Hillenbrand, Science **313**, 1595 (2006).
[110] P. Li, T. Wang, H. Böckmann, and T. Taubner, Nano Lett. **14**, 4400 (2014).